



Synergetic modulation of molecular oxygen activation and surface acidity/basicity on defective M/Uio-66m (M = Pt, Pd) for advanced oxidation of gaseous formaldehyde at room temperature

Yifan Zhuo, Xiuling Guo, Wei Cai, Tao Shao, Dehua Xia, Chuanhao Li, Shengwei Liu*

School of Environmental Science and Engineering, Guangdong Provincial Key Laboratory of Environmental Pollution Control and Remediation Technology, Sun Yat-sen University, Guangzhou 510006, PR China

ARTICLE INFO

Keywords:

Electronic metal support interaction (EMSI)
Coordinatively unsaturated Zr-sites (Zr-CUSs)
Molecular oxygen (O_2) activation
Formaldehyde (HCHO)
Metal-organic frameworks (MOFs)

ABSTRACT

Molecular oxygen (O_2) dominated room temperature catalytic oxidation (RTCO) technique is essential for removing indoor formaldehyde (HCHO) and guaranteeing indoor air safety. However, RTCO is challenged by low O_2 activation efficiency and uncontrollable O_2 activation pathway. In this study, defective UiO-66 (UiO-66m) with abundant coordinatively unsaturated Zr-sites (Zr-CUSs) is exploited for anchoring well-dispersed noble metals (M = Pt, Pd) and tuning surface acidity/basicity. The strong interfacial electronic metal support interactions at Zr-CUSs–M active centers trigger O_2 activation into mobile ROS (superoxide radicals ($\bullet O_2^-$), singlet oxygen (1O_2)) at room temperature. Consequently, adsorbed HCHO can be efficiently oxidized into CO_2 with exceptional mineralization efficiency (over 90%) and considerable recyclability (6 runs, 6 h). A novel ROS-initiated advanced oxidation pathway, together with the synergetic acid/base catalytic effects, is proposed based on *in situ* spectroscopic studies. This study will provide new insights into the O_2 activation pathway and designing advanced RTCO catalysts.

1. Introduction

Formaldehyde (HCHO), a prevalent volatile organic compound (VOC), is a highly detrimental indoor air pollutant, primarily originating from wood-based furnishing and building materials. The concentration of HCHO in indoor air usually ranges from ppb to sub-ppm, sometimes reaching several hundred ppm under strong source activities, frequently exceeding the guideline maximum value (0.1 mg/m^3) of the World Health Organization [1,2]. Moreover, people spend increased time staying indoors (80–90%), especially during the Coronavirus disease (COVID-19) pandemic period. Long-term exposure to HCHO can result in respiratory irritation, pneumonia, and even cancer. In 2017, HCHO was again classified as a Group 1 carcinogen by The International Agency for Research on Cancer [2]. To guarantee indoor air safety, considerable efforts have been made to remove indoor HCHO by various techniques, such as adsorption, photocatalytic oxidation, plasma-catalytic oxidation, and room temperature catalytic oxidation (RTCO) [3,4].

To date, RTCO is one of the most promising techniques to remove indoor formaldehyde, owing to the advantages of moderate operation

conditions, low operation cost, and minimizing secondary pollution. Developing a highly efficient RTCO catalyst is essential for the practical application of the RTCO technique. Among various available RTCO catalysts (e.g., Pt or Pd/TiO₂, MnO_x), supported noble metal catalysts are intensively investigated [5,6]. However, their activity in terms of HCHO removal efficiency, mineralization efficiency, and recyclability still cannot meet the practical requirements for treating HCHO in indoor air characterized by high airflow but low HCHO concentration. What is worse, low activity is usually accompanied by the gradual accumulation of reaction intermediates (e.g., formate species and/or carbonate species) and the deactivation of catalysts [2,7]. For example, it was reported that the conversion of formate intermediates, one of the major rate-determining steps for the catalytic HCHO degradation, was retarded and thus accumulated on the Pt/TiO₂ catalyst surface [8]. In essence, the activity of most reported supported noble metal catalysts, including the intensively studied Pt or Pd/TiO₂, is restricted by low O_2 activation efficiency and uncontrollable O_2 activation pathway. In the heterogeneous catalytic oxidation process, various forms of activated oxygen species have been observed to be involved in reactions such as O_2 (adsorbed), O_2^- (superoxide), O_2^{2-} (peroxide), O_2^{2-} (lattice oxygen)

* Corresponding author.

E-mail address: liushw6@mail.sysu.edu.cn (S. Liu).

<https://doi.org/10.1016/j.apcatb.2023.122789>

Received 27 February 2023; Received in revised form 10 April 2023; Accepted 19 April 2023

Available online 20 April 2023

0926-3373/© 2023 Elsevier B.V. All rights reserved.

and OH (active hydroxyl groups) [9,10]. The production of those active oxygen species is reliant on particular pathways for activating O₂. Up to now, there are mainly two different kinds of proposed O₂ activation pathways on supported noble metal catalysts. One is the adsorption-dissociation activation pathway, in which the active centers are the supported noble metal species, where the adsorbed O₂ molecules are typically split into two active O atoms. Another is the oxygen vacancy activation pathway, in which the active centers are the defective support with abundant oxygen vacancies, where the adsorbed O₂ is converted into active lattice oxygen that participated in the catalytic reactions via the Mars-Van Krevelen (MVK) mechanism. Nevertheless, the reactivity and mobility of active surface/lattice oxygen are still limited, and activating molecular oxygen into more reactive and mobile oxygen radicals at room temperature on supported noble metal catalysts remains a great challenge [10].

Essentially, the activity of supported noble metal catalysts for O₂ activation and HCHO degradation is modulated by a variety of compositional and structural parameters of noble metal nanoparticles (NPs), as well as the nature of support materials and their interfacial metal-support interactions. In particular, to improve the activity of supported noble metal catalysts, diverse modifying approaches, such as heteroatom doping, H₂ reduction, facet engineering, have been advanced to exploit the metal/support synergetic effects [11–13]. Tuning the metal-support interactions will not only help to control the traits of supported noble metal NPs, including size, dispersion, electronic structures, etc., but also affects the defects, bonding environments/strength, lattice oxygen mobility, and surface acidity/basicity of the support materials [14]. Significantly, the electronic structures (chemical states and d-band center) of noble metal active centers can be adjusted by establishing tunable electronic metal support interaction (EMSI) [15–17]. By tuning the EMSI, the adsorption configuration, adsorption strength, and surface coverage of molecular oxygen on noble metal active centers with varied electronic structures as well as the electron transfer at the O₂ and noble metal interface will be regulated [18–20]. In this sense, tuning the EMSI is an effective method to regulate the adsorption and activation of molecular oxygen [21]. Besides, the strong EMSI effect is beneficial to stabilize the supported noble metal nanoparticles with high dispersion. Tuning EMSI can be readily achieved by modulating the nature of support materials, for example, introducing coordinatively unsaturated sites and building interfacial coordination interactions. In particular, defect engineering of support materials is widely employed to introduce coordinatively unsaturated sites, and thus to tune the EMSI effect and to modulate the electronic structures of supported noble metal catalysts.

Metal-organic frameworks (MOFs) as outstanding support materials are characteristic of high surface areas and highly porous frameworks, which are beneficial for uniform immobilization of noble metal NPs on the surface and in the bulk, superior to the commonly used metal oxide (TiO₂, Al₂O₃, etc.) only providing surface sites. Among various MOFs, highly porous UiO-66 (Zr₆(μ₃-O)₄(μ₃-OH)₄(BDC)₆, BDC = benzene-1,4-dicarboxylate) is intensively investigated, owing to abundant functionalities and excellent thermal/chemical stability [22–24]. Within the pristine UiO-66 framework, a Zr₆(μ₃-O)₄(μ₃-OH)₄ octahedron (Zr₆-cluster) is connected to neighboring Zr₆-cluster through carboxylate groups (–CO₂) from BDC linkers, forming a 12-fold bridge. Each zirconium atom in the Zr₆(μ₃-O)₄(μ₃-OH)₄(BDC)₆ cluster has eight coordinating oxygen atoms from the –CO₂, μ₃-O, and μ₃-OH groups [25]. In this sense, the Zr₆-clusters in pristine UiO-66 are partitioned by BDC ligands and show weak interaction with the immobilized guest noble metal NPs. To enhance the EMSI effect, many strategies, including post-synthetic modification and adding organic modulators, have been adopted to introduce missing linker/cluster defects and generate coordinatively unsaturated sites (CUSs), without virtual changes in the overall framework [26]. For example, Behm et al. employed acetic acid as a modulator to introduce Zr-CUSs in UiO-66 and to immobilize single-atom Cu, resulting in a strong EMSI effect and superior catalytic

performances [27]. Trifluoroacetic acid (TFA), with pK_a = 0.23, is one of the most efficient modulators to introduce missing cluster/linker defects in UiO-66 with tunable Zr-CUSs [28]. After TFA modulation, the specific surface area can be increased and more mesopores will be introduced, facilitating the mass transfer. The synergy between high porosity and abundant Zr-CUSs within TFA-modulated defective UiO-66 will endow it with great potential for uniformly immobilizing noble metal catalysts with a strong EMSI effect.

In this study, TFA-modulated defective UiO-66 (UiO-66m) were synthesized for immobilizing Pt catalyst with good dispersion and strong EMSI effect (Scheme 1). Significantly, it was found that Pt/UiO-66m with a strong EMSI effect contributed to the enhanced O₂ adsorption and activation, generating mobile reactive oxygen species (ROS), including superoxide radicals (•O₂[–]) and singlet oxygen (¹O₂). Accordingly, the RTCO performance of HCHO degradation was significantly improved with superior stability, compared to Pt/UiO-66. A similar phenomenon can be also observed for UiO-66m supported Pd catalysts. Moreover, a novel ROS-initiated advanced oxidation pathway, together with the synergetic acid/base effects, is proposed for RTCO of HCHO, based on *in situ* spectroscopic studies. This work will enlighten a feasible strategy for exploiting advanced supported noble metal catalysts accelerating efficient O₂ activation for indoor air purification at room temperature.

2. Experimental section

2.1. Preparation of M/UiO-66 and M/UiO-66m (M = Pt, Pd)

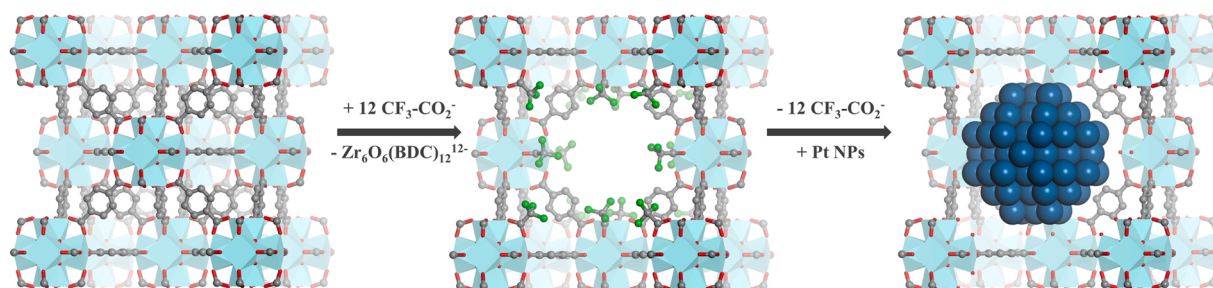
UiO-66 was synthesized by the typical solvothermal method [24]. UiO-66m was fabricated by adding a suitable dosage of TFA as a modulator under otherwise identical conditions. M/UiO-66 and M/UiO-66m were synthesized by NaBH₄-mediated chemical reduction method in the ice bath. The nominal weight ratios of noble metals on support materials were 1 wt%. More details about the preparation of UiO-66, UiO-66m, M/UiO-66, and M/UiO-66m were elaborated in Text S1 in the supplementary material.

2.2. Measurement of catalytic activity

For the static activity test, the HCHO removal performance experiments were carried out in a homemade box reactor, using 0.1 g catalyst. When the HCHO concentration in the air reached equilibrium (115 ± 5 ppm, relative humidity (RH) = 30 ± 3%, for comparison, an initial concentration of about 7.5 or 210 ppm was also studied), the reaction was initiated. To study the effect of RH on the HCHO removal performance, Pt/UiO-66m catalyst was tested at different RH values (5–75%). To remove the residual substances on the Pt/UiO-66m surface after 5 cycles, the sample was washed with water and dried at 60 °C air for 12 h before the next cycle test. The concentrations of HCHO, CO, CO₂, and H₂O were monitored by Photoacoustic Gas Monitor (INNOVA 1412i) every minute.

For the dynamic activity test, a high-temperature reaction chamber (Harrick) was used as the fixed bed. 0.02 g of catalyst was placed on a 250 × 250 mesh screen in the sample cup of the reaction chamber. The flow and concentration of HCHO were modulated by a polytetrafluoroethylene bypass tube. First, a gas mixture of HCHO (115 ppm or 8 ppm) and synthetic air (21% O₂ and 79% N₂) flowed into the bypass tube with a total gas flow of 2000 mL·h^{–1}. Then, the gas flow with a gas hourly space velocity (GHSV) of 100,000 mL·g^{–1}·h^{–1} was switched to the reaction chamber and the reaction was initiated. The RH value was 30 ± 3% throughout the test. The concentration of HCHO, CO, CO₂, and H₂O were monitored by the Photoacoustic Gas Monitor.

In all the experiments, the removal and mineralization efficiency were calculated using the following equations:



Scheme 1. Schematic illustration of the synthetic process of Pt/UIO-66m. (C: grey; O: red; Zr: cyan; F: green; Pt: blue; H atoms are omitted for clarity).

$$\text{Removal (\%)} = \left(1 - \frac{C_t}{C_0}\right) \times 100\% \quad (1)$$

$$\text{Mineralization (\%)} = \left(\frac{\Delta\text{CO}_2}{\Delta\text{CO}_2 + C_t}\right) \times 100\% \quad (2)$$

where C_0 and C_t were the initial and a certain time of HCHO concentration (ppm), respectively. ΔCO_2 represented the difference between the stable concentration and initial concentration of CO_2 .

2.3. Characterization and computational details

The thermal stability, defects, and surface acidity/basicity of the samples were characterized by thermo-gravimetry and differential scanning calorimetry (TG-DSC) analyses, Fourier transform infrared

spectroscopy (FTIR), NH_3 temperature programmed desorption (NH_3 -TPD), and CO_2 -TPD. The composition, structures, and physiochemical properties were analyzed by X-ray diffractometer (XRD) patterns, nitrogen sorption isotherms, scanning electron microscopy (SEM) images, transmission electron microscopy (TEM) images, high-resolution TEM (HRTEM) images, high-angle annular dark-field scanning TEM (HAADF-STEM) images, zeta potential analysis, X-ray photoelectron spectroscopy (XPS), O_2 -TPD, hydrogen temperature programmed reduction (H_2 -TPR) curves, inductively coupled plasma atomic emission spectrometer (ICP-AES), *in situ* diffuse reflectance infrared Fourier transform spectroscopy (DRIFTS) of CO adsorption and pulse CO chemisorption. HCHO removal performances and mechanism of the samples were characterized by electron paramagnetic resonance (EPR) and *in situ* DRIFTS. DFT calculations were performed with the CP2K package. The additional details and computational details were described in Text S2.4.

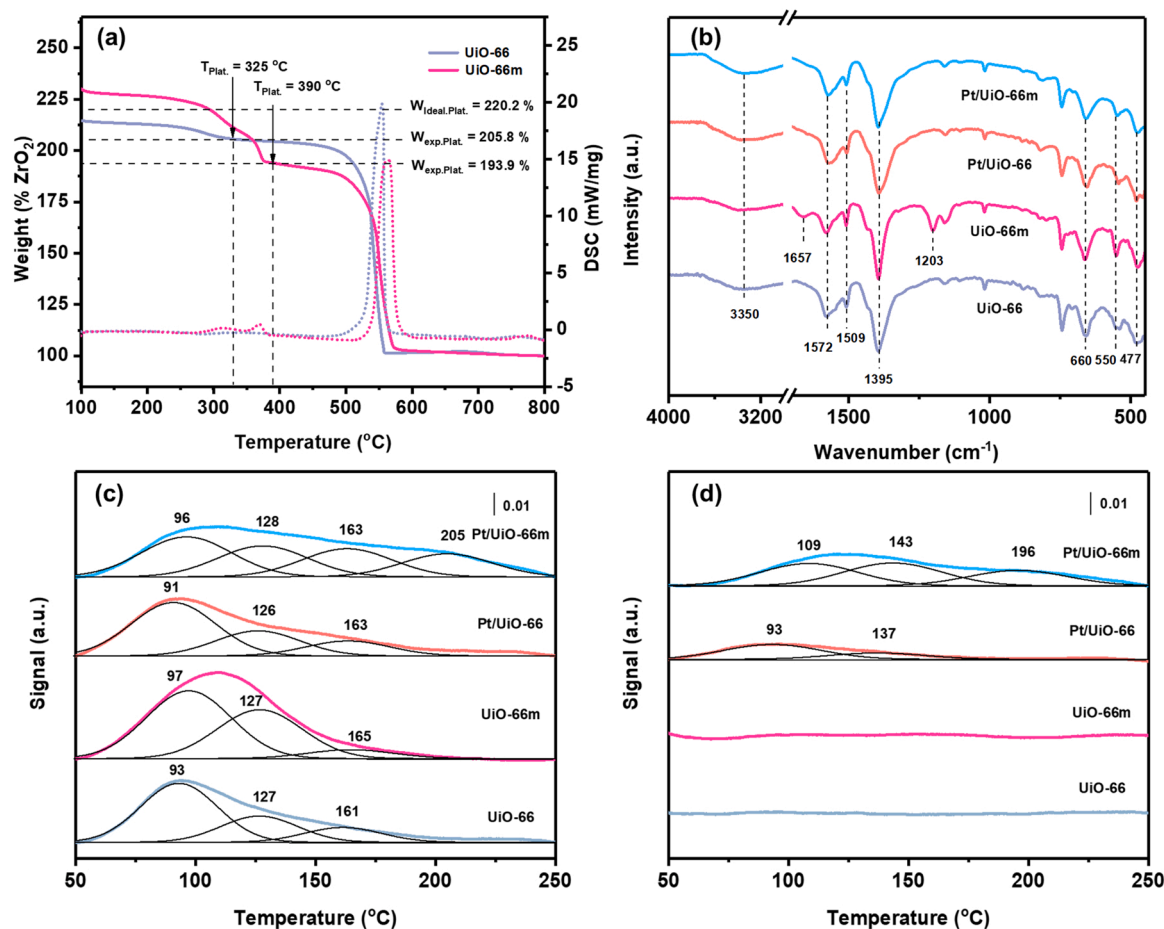


Fig. 1. (a) TG-DSC analyses of UiO-66 and UiO-66m, (b) FTIR spectra, (c) NH_3 -TPD profiles, and (d) CO_2 -TPD profiles of UiO-66, UiO-66m, Pt/UIO-66, and Pt/UIO-66m.

3. Results and discussion

3.1. Surface chemistry of Pt/Uio-66m catalysts

The chemical formula of defect-free UiO-66 is $[\text{Zr}_6(\mu_3\text{-O})_4(\mu_3\text{-OH})_4(\text{BDC})_6]$. Compared to the majority of MOFs, UiO-66 exhibits greater stability due to its robust Zr–O bonding and high coordination number between the Zr_6 -clusters and BDC linkers. Without defect modulation, only a low concentration of terminal Zr-CUSs exists in pristine UiO-66 samples. TG-DSC can be performed to estimate the concentration of missing linker defects (Fig. 1a and Text S2.5). In the present study, calculated by TGA result, pristine UiO-66 contains about 0.72 missing BDC linkers per Zr_6 -cluster in chemical formula (that is, $5.28 \times 2 = 10.56$ BDC linkers are coordinated to Zr_6 -cluster in the structural model). TFA modulation is effective in introducing missing linker defects in the UiO-66 framework. Upon TFA modulation with suitable dosage ($\text{H}_2\text{BDC}/\text{TFA} = 1/12$) in the present study, the amount of missing linker defects in defective UiO-66m increased to 1.31 missing linkers per Zr_6 -cluster in chemical formula (that is, $4.69 \times 2 = 9.38$ BDC linkers are coordinated to each Zr_6 -cluster in the structural model). In comparison to the Zr_6 -cluster of pristine UiO-66, after TFA modulation, around 0.59 BDC linker per Zr_6 -cluster in the chemical formula is substituted in defective UiO-66m, forming additional Zr-CUSs that are otherwise capped by trifluoroacetate groups (deprotonated TFA) or water molecules ($-\text{OH}/-\text{OH}_2$).

FTIR spectra (Fig. 1b) were conducted to further explore the functional groups of the prepared samples. Before and after TFA modulation, the structural framework of UiO-66 was retained. The Zr_6 -clusters presented three characteristic peaks at 550, 660, and 477 cm^{-1} , which were attributed to asymmetric stretching of $\text{Zr}-(\text{O}_2\text{C})$, $\mu_3\text{-O}$, and $\mu_3\text{-OH}$, respectively [29]. The BDC ligands also presented three characteristic peaks. The bands at 1395 cm^{-1} and 1572 cm^{-1} are assigned to symmetric and asymmetric vibration of $\text{O}=\text{C}-\text{O}$ for the carboxylate group in BDC, respectively. The band at 1509 cm^{-1} is assigned to the $\text{C}=\text{C}$ stretching vibration of the aromatic ring [30]. The large broad band at 3350 cm^{-1} is attributed to the H-bonded OH groups of residual water [31]. Notably, after TFA modulation, two new peaks at 1203 cm^{-1} and 1657 cm^{-1} were detected for UiO-66m, which were attributed to anti-symmetrical stretching vibrations of C–F bonds and stretching vibration of $\text{O}=\text{C}-\text{O}$ from the TFA modulator, respectively [32,33]. Upon TFA modulation, missing linker/cluster defects were introduced and Zr-CUSs were formed in UiO-66m, which were then partially stabilized by adsorbing capping agents, including TFA and/or H_2O . Interestingly, after Pt loading, the newly emerged two peaks in UiO-66m disappeared, implying that the Zr-CUSs linked trifluoroacetate groups are substituted by $-\text{OH}/-\text{OH}_2$ through hydrolysis reactions (Fig. S1), which provide active sites for anchoring Pt NPs.

NH_3 -TPD and CO_2 -TPD were performed to study the variation in acid-base characteristics before and after surface modulations. According to the TG result (Fig. 1a), the Zr_6 -clusters of UiO-66 and UiO-66m are dehydroxylated/decomposed above 250 $^\circ\text{C}$, so the NH_3 -TPD and CO_2 -TPD data were collected just below 250 $^\circ\text{C}$. For pristine UiO-66 and defective UiO-66m, broad NH_3 desorption peaks in the range of 50–200 $^\circ\text{C}$ were recorded, which can be fitted into three peaks (Fig. 1c). The peaks at around 93–97 $^\circ\text{C}$ and 126–128 $^\circ\text{C}$ are attributed to Bronsted acid of Zr–OH and Zr–OH₂, respectively, which are originated from surface adsorbed water at the Zr-CUSs, and the peak at 163 $^\circ\text{C}$ is assigned to bridging $\mu_3\text{-OH}$ (Zr–OH–Zr) in the bulk of Zr_6 -clusters [34]. After TFA modulation, compared to pristine UiO-66 (18.01 cm^3/g), the total acid density of defective UiO-66m (31.15 cm^3/g) is larger based on the integral area of the NH_3 desorption peak, owing to more Zr-CUSs in defective UiO-66m to adsorb and activate water molecules to form more Bronsted acid sites of $-\text{OH}/-\text{OH}_2$ (Table S1). After Pt loading, the acid density of Pt/UiO-66 (18.27 cm^3/g) is basically unchanged, suggesting the weak interaction between Pt and UiO-66. In contrast, for Pt/UiO-66m, the acid density attributed to $-\text{OH}/-\text{OH}_2$ became smaller,

suggesting that Zr–OH/Zr–OH₂ (that is, the water capped Zr-CUSs sites) are partially occupied by Pt NPs. Meanwhile, the NH_3 desorption peak is extended to a higher temperature and a new peak at 205 $^\circ\text{C}$ can be fitted, which can be attributed to the formation of Zr–OH–Pt at the interface. In this connection, after Pt loading, a portion of terminal hydroxyls (OH_t) is transformed into bridging hydroxyls (OH_b), which is further supported by DRIFTS study (Fig. S1b). Zr-CUSs is a kind of strong Lewis acid ($\text{pK}_a = -0.3$), and Zr-CUSs can be stabilized upon Pt deposition, the new 205 $^\circ\text{C}$ -peak can also be partially related to Zr-CUSs–Pt sites [34]. The NH_3 desorption peaks for Pt/UiO-66m are broader and the total acidity density (31.15 cm^3/g) is nearly 1.5 times that of UiO-66m, suggesting that more acid sites were formed upon removing trifluoroacetate groups.

Relatively, the surface of basicity is much weaker. As shown in Fig. 1d, no obvious peaks were recorded over UiO-66 and UiO-66m. During the NaBH_4 -mediated Pt deposition process, a portion of acid sites was deprotonated. After Pt loading, a broad CO_2 desorption peak in the range of 50–175 $^\circ\text{C}$ was recorded over Pt/UiO-66, which can be fitted into two peaks. The weak CO_2 desorption peaks at 93 $^\circ\text{C}$ are assigned to Zr–OH, deprotonated from Zr–OH₂. The peak at 137 $^\circ\text{C}$ is attributed to $\text{Zr}-\text{O}^-$, transformed from deprotonating Zr–OH. For Pt/UiO-66m, the CO_2 desorption peaks attributed to Zr–OH and $\text{Zr}-\text{O}^-$ shifted to a higher temperature, at 109 and 143 $^\circ\text{C}$, indicating the increased basicity. Notably, a new peak corresponding to Bronsted basic sites appeared at 196 $^\circ\text{C}$, which may be associated with Zr–O–Pt linkage, transforming from Zr–OH–Pt via deprotonation. Of course, basic Zr–O–Pt sites may be also derived from Zr-CUSs–Pt via O_2 adsorption and activation. Compared to Pt/UiO-66 (4.94 cm^3/g), the total basic density of defective Pt/UiO-66m (8.66 cm^3/g) is larger based on the integral area of the CO_2 desorption peak over Pt/UiO-66m. This finding is supported by the Zeta potential result, which shows that the isoelectric point (pH_{IEP}) of Pt/UiO-66m (5.44) is higher than that of Pt/UiO-66 (4.86) (Fig. S2). Compared to Pt/UiO-66, the positive shift of pH_{IEP} observed on Pt/UiO-66m would indicate the more basic surface.

Overall, surface acidity/basicity on defective Pt/UiO-66m can be tuned by combinative TFA modulation and Pt loading. After TFA modulation, more Zr-CUSs were introduced, and more H_2O were adsorbed and activated, leading to higher acid density of UiO-66m. During the NaBH_4 -mediated Pt deposition process, the Zr-CUSs bound trifluoroacetate groups will be substituted by $-\text{OH}/-\text{OH}_2$, which can further increase the acid density. Meanwhile, some acidic sites were converted into basic sites by deprotonation. Notably, those Zr-CUSs derived acidic sites in UiO-66m were active sites for anchoring Pt, and diverse linkage configuration (Fig. 2), including Zr–OH–Pt, Zr-CUSs–Pt and Zr–O–Pt, were formed at the interface between Pt NPs and defective UiO-66m. As a consequence, a portion of bridging hydroxyls (OH_b) are formed in Pt/UiO-66m, increasing the strength of surface acidity. Meanwhile some Lewis acidic Zr-CUSs are stabilized by Pt shielding, leaving to O_2 adsorption and activation, giving rise basic Zr–O–Pt and/or active oxygen species (as will be elaborated later). The modulated surface acidity and basicity will help accelerate the transformation of HCHO into DOM and formate species through acid-base catalysis [35].

3.2. EMSI effects in Pt/UiO-66m catalysts

The BET surface area (S_{BET}), pore volume (V_{pore}), and pore size distribution (PSD) were analyzed by the N_2 sorption isotherms (Fig. S3). All the catalysts possessed type I isotherms, characteristic of microporous structures. Upon TFA modulation, because of the lower pK_a and large concentration of TFA, trifluoroacetate groups would outcompete BDC for binding to Zr_6 -clusters. As BDC was substituted by trifluoroacetate groups with smaller molecular size, larger pore space and higher pore volume was left in UiO-66m, leading to significantly higher S_{BET} (1566.7 m^2/g) and V_{pore} (0.34 cm^3/g) of UiO-66m (Table 1). Meanwhile, more Zr-CUSs are introduced together with high population of large pore size in UiO-66m, approximately 2–3 nm (Fig. S3b) [28]. During the NaBH_4 -mediated deposition of Pt NPs, trifluoroacetate

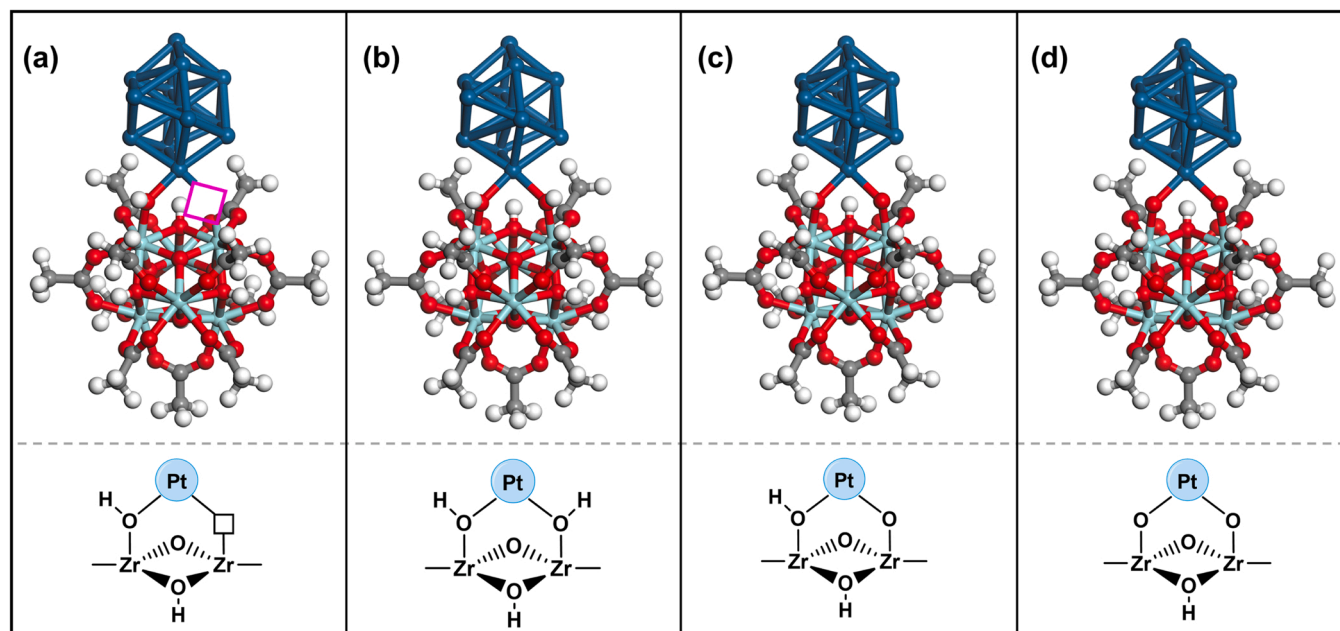


Fig. 2. The different connection between Pt NPs and support in Pt/Uio-66m using Pt₁₃/Uio-66m models as examples (C: grey; O: red; Zr: cyan; Pt: blue; H: white; squares: Zr-CUSs).

Table 1

BET surface area, Pt content, Pt dispersion, and turnover frequency (TOF) of Uio-66, Uio-66m, Pt/Uio-66, and Pt/Uio-66m.

Samples	S _{BET} (m ² /g)	V _{pore} (cm ³ /g)	Pt content (%)	Pt dispersion (%)	TOF × 10 ⁻¹ (s ⁻¹)
Uio-66	869.8	0.15	–	–	–
Uio-66m	1566.7	0.34	–	–	–
Pt/Uio-66	793.9	0.076	0.89	37.48	1.17
Pt/Uio-66m	887.2	0.084	0.91	46.45	2.52

Note: S_{BET}: BET surface area; V_{pore}: pore volume; Pt content determined by ICP-AES; Pt dispersion measured by CO pulse chemisorption; TOF calculated by equation S1 in supplementary material (S2.2).

groups will be removed by hydrolysis reactions, and more bigger pores will be available for inward mass transport of PtCl₆²⁻ precursors. Moreover, as shown in Fig. S2, the isoelectric point (pH_{IEP}) value of Uio-66 is 4.49, while pH_{IEP} for TFA-modulated Uio-66m increases to 6.90. In this sense, Uio-66m favor for adsorbing negatively charged PtCl₆²⁻, compared to Uio-66. Together, Uio-66m, with higher S_{BET}, accessible larger pore tunnel and weaker electrostatic repulsion, facilitated the uniform deposition of Pt NPs with higher dosage. As a result, the S_{BET} and V_{pore} of Pt/Uio-66m decreased significantly, suggesting that Pt NPs were uniformly deposited on both the surface and the cavities of Uio-66m framework. In contrast, the decrease in S_{BET} and V_{pore} of Pt/Uio-66 are not as intensive in Uio-66, suggesting that Pt NPs were mainly deposited on the external surface of Uio-66.

The TFA modulation and loading of Pt NPs did not destroy the basic framework of Uio-66, and the XRD patterns (Fig. S4) for all samples displayed comparable peaks at 7.4°, 8.5°, and 25.8°, which corresponded to the (111), (200), and (600) planes of Uio-66 [22]. Unfortunately, the signal for Pt were not recorded, due to the high dispersion and low loading concentration. By ICP-AES analysis, as shown in Table 1, Pt/Uio-66 and Pt/Uio-66m had Pt content of 0.89 wt% and 0.91 wt%, respectively. The morphology and microstructures of the samples were characterized by electron microscopy. According to Fig. S5a, Uio-66 exhibits a typical cubic structure with an average width of about 100 nm. TFA modulation did not affect the particle size, but

induced Uio-66m evolving into quasi-spherical morphology (Fig. S5b), due to surface capping effects of TFA. After Pt loading, the morphology of support is retained (Fig. S5c, d). But, the different textural nature and surface chemistry of Uio-66 and TFA-modulated Uio-66m lead to the different distribution of loaded Pt NPs. As shown in the HAADF-STEM and TEM images (Fig. 3a, b and Fig. S6), Pt NPs are predominantly situated on the exterior of Uio-66, whereas they are located both on the external surface and within the pores of Uio-66m. The Pt dispersion can be estimated by CO pulse chemisorption analysis, and the values for the Pt/Uio-66 and Pt/Uio-66m catalysts are 37.48% and 46.45%, respectively. The size of loaded NPs in Pt/Uio-66m are 2–3 nm. In the HRTEM images, the resolved lattice fringes with a spacing of about 0.22 nm can be observed, which corresponded to the Pt (111) plane (Fig. 3c, d).

XPS measurements were performed to examine the surface elemental composition and chemical states of Pt. The full survey spectra for all samples showed the presence of Zr, C, and O, while F was only detected in Uio-66m (Fig. S7). In the Zr 3d spectrum for Uio-66 (Fig. 4a), a pair of peaks centered at 185.17 and 182.77 eV were correlated to Zr 3d_{3/2} and Zr 3d_{5/2} of Zr⁴⁺. After TFA modulation, more Zr-CUSs were introduced, some BDC ligands was substituted by trifluoroacetate groups and/or –OH group with higher electronegativity, and the binding energy of Zr increased. In contrast, after loading Pt NPs, the binding energy of Zr 3d in Pt/Uio-66 decreased by 0.13 eV, suggesting the electron transfer from deposited Pt NPs to the Zr₆-cluster. In comparison, for Pt/Uio-66, the shift in binding energy (Δ = 0.23 eV) was larger, indicating stronger EMSI between Pt and Uio-66m. The O 1s peaks were deconvoluted into three branches that are assigned to the Zr–O–Zr (530.40 eV), Zr–O–C (531.80 eV), and Zr–OH/OH₂ (532.90 eV) (Fig. 4b) [36]. After TFA modulation, more H₂O adsorbed and activated at Zr-CUSs, and the content of Zr–OH/OH₂ increased from 13.5% to 18.3% (Table S2). After loading Pt NPs, the percentage of Zr–OH/OH₂ in Pt/Uio-66 (10.4%) and Pt/Uio-66m (11.2%) decreased, and Zr–O–OH–Pt bond was newly formed, being consistent with the NH₃-TPD result. Due to the EMSI, the loaded Pt exhibited two distinct chemical states (Fig. 4c). The peaks at 71.13 and 71.60 eV are assigned to Pt⁰, and the other peaks at 72.88 and 72.90 eV can be assigned to positively charged Pt^{δ+} species [37]. Obviously, more Pt^{δ+} species are formed in Pt/Uio-66m, compared to that in Pt/Uio-66, suggesting stronger EMSI between Pt NPs and defective Uio-66m. Using CO as probe molecule, DRIFTS spectroscopy

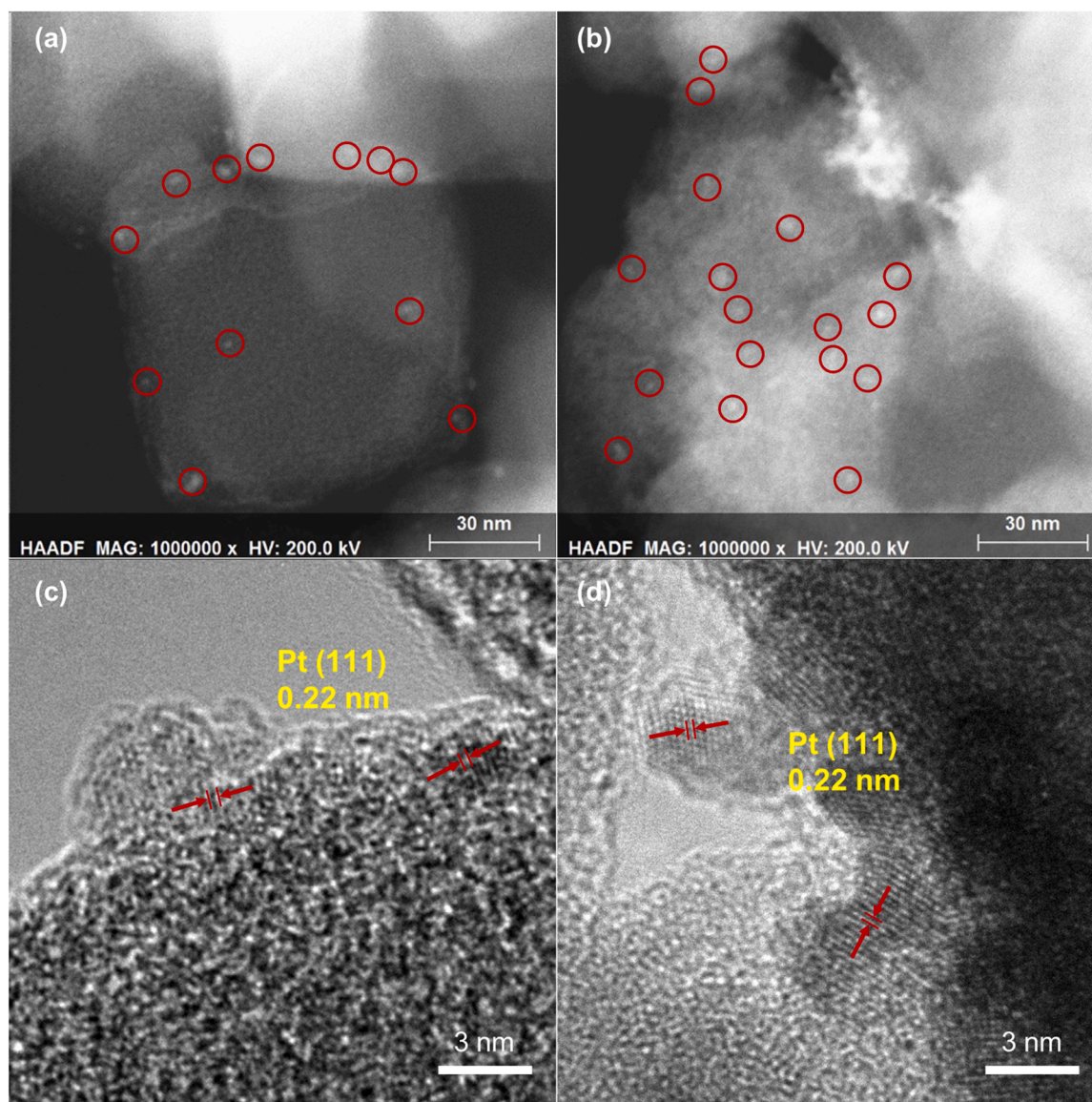


Fig. 3. HAADF-STEM images of (a) Pt/Uio-66 and (b) Pt/Uio-66m, and HRTEM image of (c) Pt/Uio-66 and (d) Pt/Uio-66m.

(Fig. 4d) further confirmed the existence of intensive positively charged $\text{Pt}^{\delta+}$ species in Pt/Uio-66m. The characteristic CO adsorption peaks at 2049 cm^{-1} (Pt/Uio-66) or 2055 cm^{-1} (Pt/Uio-66m) were ascribed to linearly adsorbed CO on Pt^0 NPs. An additional 2083 cm^{-1} peaks for Pt/Uio-66m was ascribed to CO adsorbed on $\text{Pt}^{\delta+}$ species [38]. By the way, the lack of any detectable peak between 1920 and 1950 cm^{-1} suggests that bridged-adsorbed CO is not present on the Pt NPs, implying the high dispersion of Pt species [39]. A similar XPS and CO-DRIFTS results were also recorded over Pd/Uio-66m (Fig. S8).

In short, after TFA modulation, more Zr-CUSs were introduced, providing more sites for adsorbing and activating H_2O , and anchoring noble metals with interfacial Zr-O/OH-Pt bonding and stronger EMSI, leading to more $\text{Pt}^{\delta+}$ species over Pt/Uio-66m. Meanwhile, Uio-66m possessed higher S_{BET} , larger pore tunnel and weaker electrostatic repulsion, exposing more accessible sites both on the surface and in the pore for uniformly anchoring of Pt NPs with higher dosage and higher Pt dispersion.

3.3. Oxygen activation over Pt/Uio-66m catalysts

The oxygen activation is crucial for HCHO oxidation. The reactivity

and activation of oxygen species were determined by H_2 -TPR and O_2 -TPD. For pristine Uio-66, no obvious H_2 consumption and O_2 desorption peaks were emerged (Fig. 5a, b), indicating that the surface oxygen of Uio-66 is almost inert. After TFA modulation, a H_2 consumption peak emerged at $-3\text{ }^\circ\text{C}$, which may be attributed to the reduction of surface adsorbed O_2 at exposed Zr-CUSs ($\text{Zr-CUSs-O}_2/\text{O}_2^-$). Accordingly, an O_2 desorption peak was emerged at $153\text{ }^\circ\text{C}$. By loading Pt NPs on Uio-66, a H_2 consumption peak at $33\text{ }^\circ\text{C}$ is observed, which is related to the active oxygen adsorbed on Pt NPs [40], corresponding to an O_2 desorption peak at $80\text{ }^\circ\text{C}$ [41]. For Pt/Uio-66m, TFA was removed and more Zr-CUSs were left, which favored for adsorbing more O_2 at Zr-CUSs, and the corresponding H_2 consumption peak ($-2\text{ }^\circ\text{C}$) became larger. At the same time, because of stronger EMSI effect, more adsorbed oxygen can be activated on the surface of Pt NPs and/or at Zr-CUSs in the proximity of Pt species, and the corresponding H_2 consumption peak centered at $28\text{ }^\circ\text{C}$ was intensified. Similarly, a broad O_2 desorption peak centered at $130\text{ }^\circ\text{C}$ with much larger integral area was observed for Pt/Uio-66m, which is attributed to promoted O_2 adsorption with different configurations on the top of Pt NPs and/or at the vacancy of Zr-CUSs. Meanwhile, the reduction of $\text{Pt}^{\delta+}$ by H_2 will also contribute to H_2 consumption. Due to the EMSI-enhanced hydrogen spillover effect,

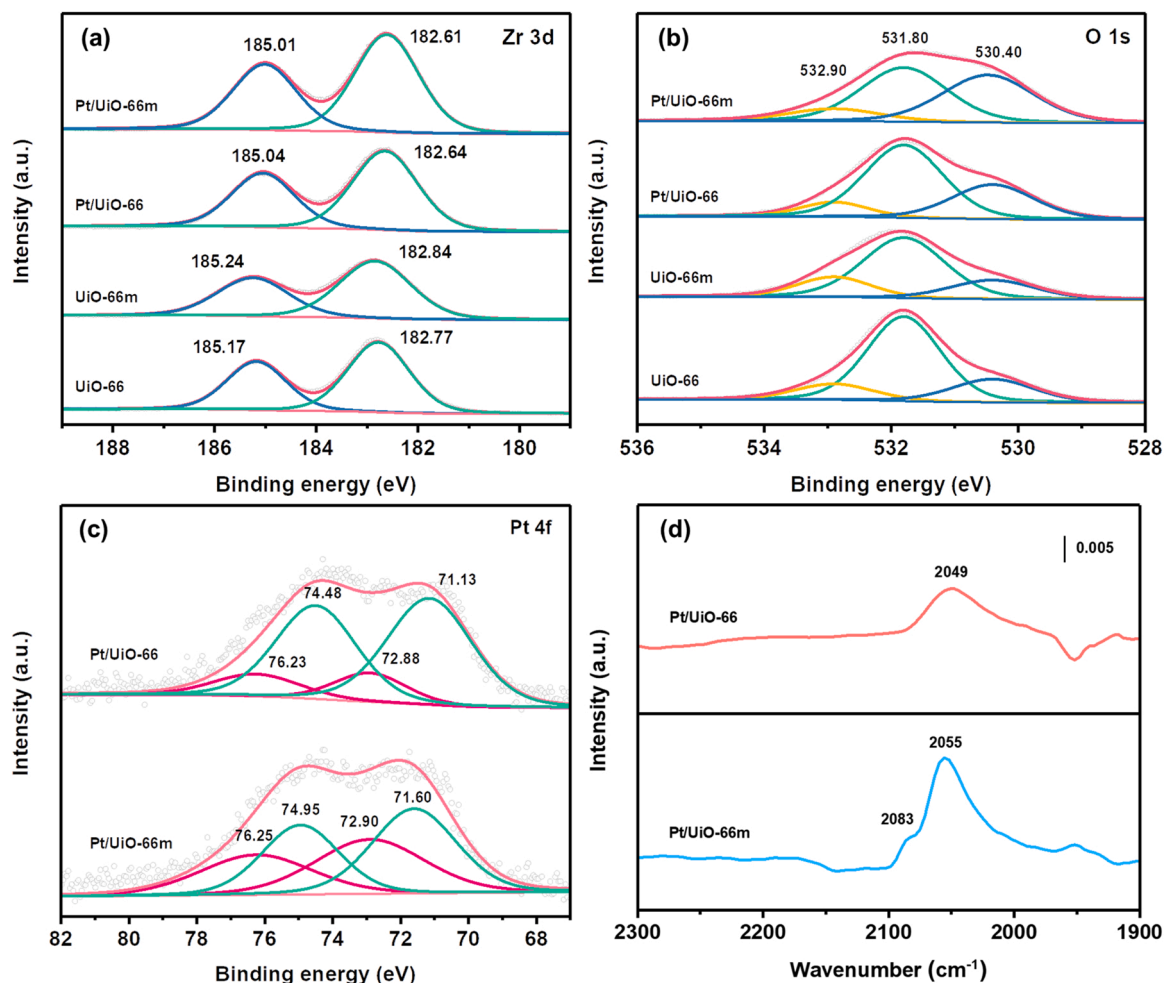


Fig. 4. High-resolution XPS spectra of (a) Zr 3d, (b) O 1 s of UiO-66, UiO-66m, Pt/UIO-66, and Pt/UIO-66m. (c) High-resolution XPS spectra of Pt 4 f of Pt/UIO-66 and Pt/UIO-66m, respectively. (d) *In situ* DRIFTS spectra of CO adsorption over Pt/UIO-66 and Pt/UIO-66m were obtained at 25 °C.

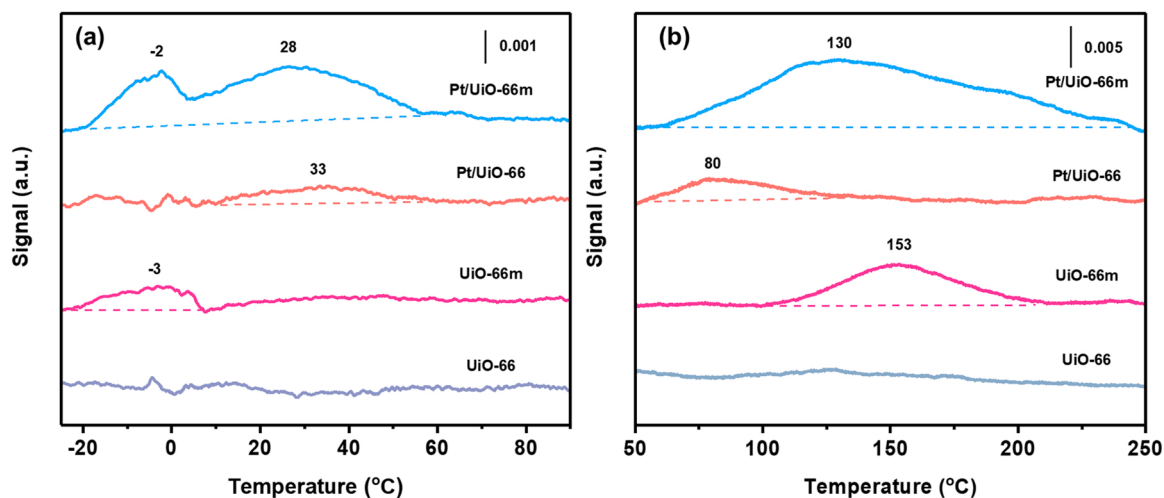


Fig. 5. (a) H₂-TPR and (b) O₂-TPD profiles of UiO-66, UiO-66m, Pt/UIO-66, and Pt/UIO-66m.

dissociated atomic hydrogen on Pt species can migrate to the UiO-66m and react with substrate oxygen species [42]. Strikingly, compared to Pt/UIO-66, the total amount of H₂ consumption on the Pt/UIO-66m catalyst was larger but the peak temperature was lower, demonstrating that the amount and reactivity of active oxygen on Pt/UIO-66m

were significantly enhanced by EMSI.

DFT calculations were conducted to explore the adsorption and activation of O₂ on the Pt species of the Pt/UIO-66m with strong EMSI and on the Pt/UIO-66 without strong EMSI. According to the above result, the computational model Pt₁₃/UiO-66m (A/B) (A and B represent

the groups (–OH, –O, or vacancy at Zr-CUSs) between Pt₁₃ and UiO-66m) and Pt₁₃ nanocluster were optimized (Fig. S9). To gain more insights into the influence on the electronic state of Pt₁₃/UiO-66m, the Bader charge was evaluated. Based on the optimized model of Pt₁₃/UiO-66m, the number of electrons transferred from Pt₁₃ to UiO-66m are calculated to be 0.85 e in Pt₁₃/UiO-66m (–OH/–OH) model, 0.40 e in Pt₁₃/UiO-66m (–OH/–O) model, and 1.42 e in Pt₁₃/UiO-66m (–O/–O) model. Subsequently, different adsorption configurations of O₂ on Pt₁₃/UiO-66m (–OH/–OH) and Pt₁₃ nanocluster were shown in Fig. 6a as well as Fig. S10, and the figure for the adsorption energy (E_{ad}) of O₂ in each configuration were shown in Table S3. According to the E_{ad} , the most favorable configuration of O₂ chemisorbed on the bridge site confined by two neighboring Pt atoms on Pt₁₃/UiO-66m (–OH/–OH) and Pt₁₃ nanocluster are observed (Fig. 6a and Fig. S10g). The corresponding adsorption energy at 298 K on Pt₁₃/UiO-66m ($E_{ad(298\text{ K})} = -3.87\text{ eV}$) is slightly lower than on Pt₁₃ nanocluster ($E_{ad(298\text{ K})} = -3.28\text{ eV}$), indicating that the interaction between O₂ and Pt₁₃/UiO-66m (–OH/–OH) is stronger than that between O₂ and Pt₁₃ nanocluster. The bond length of adsorbed molecular O₂ on Pt/UiO-66m (–OH/–OH) is slightly larger than on Pt₁₃ cluster (1.437 versus 1.409 Å), suggesting the better activation of O₂ on Pt₁₃/UiO-66m. In addition, O₂ adsorbed at Zr-CUSs–Pt

site was also calculated. Two O₂ adsorption configurations were compared. By model 1 of monodentate O₂ adsorption (Fig. 6b), the calculated magnetic moment of the chemisorbed O₂ is 0.576 μ_B and the bond length is 1.330 Å, which is similar to the properties of superoxo, while as model 2 of bidentate O₂ adsorption (Fig. S11), the calculated magnetic moment of the chemisorbed O₂ is 0 μ_B and the bond length is 1.457 Å, which is similar to the properties of peroxo [43]. In principle, it can be anticipated that the chemisorbed O₂ at the Zr-CUSs–Pt sites (site 1) is responsible for the emergence of $\bullet\text{O}_2^-$ as a result of the excitation of adsorbed O₂.

The DFT calculations indicated that the unique Zr-CUSs–Pt bonding with stronger EMSI in Pt/UiO-66m not only promoted the O₂ dissociation activation at positively charged Pt ^{$\delta+$} species, but also could enhance the electron transfer mediated activation of the molecular oxygen to generate ROSS. Such assumption was confirmed by the spin-trapping ESR results, demonstrating the formation of superoxide radicals ($\bullet\text{O}_2^-$, Fig. 6c) and singlet oxygen ($^1\text{O}_2$, Fig. 6d). Notably, ROSS were not detected with the presence of UiO-66, UiO-66m, or Pt/UiO-66 (Fig. S12a), but only on Pt/UiO-66m (Fig. 6c, d), highlight the importance of Zr-CUSs–Pt sites. Initially, O₂ can be activated into $\bullet\text{O}_2^-$ at Zr-CUSs–Pt sites via a single-electron reduction pathway, as evidenced by

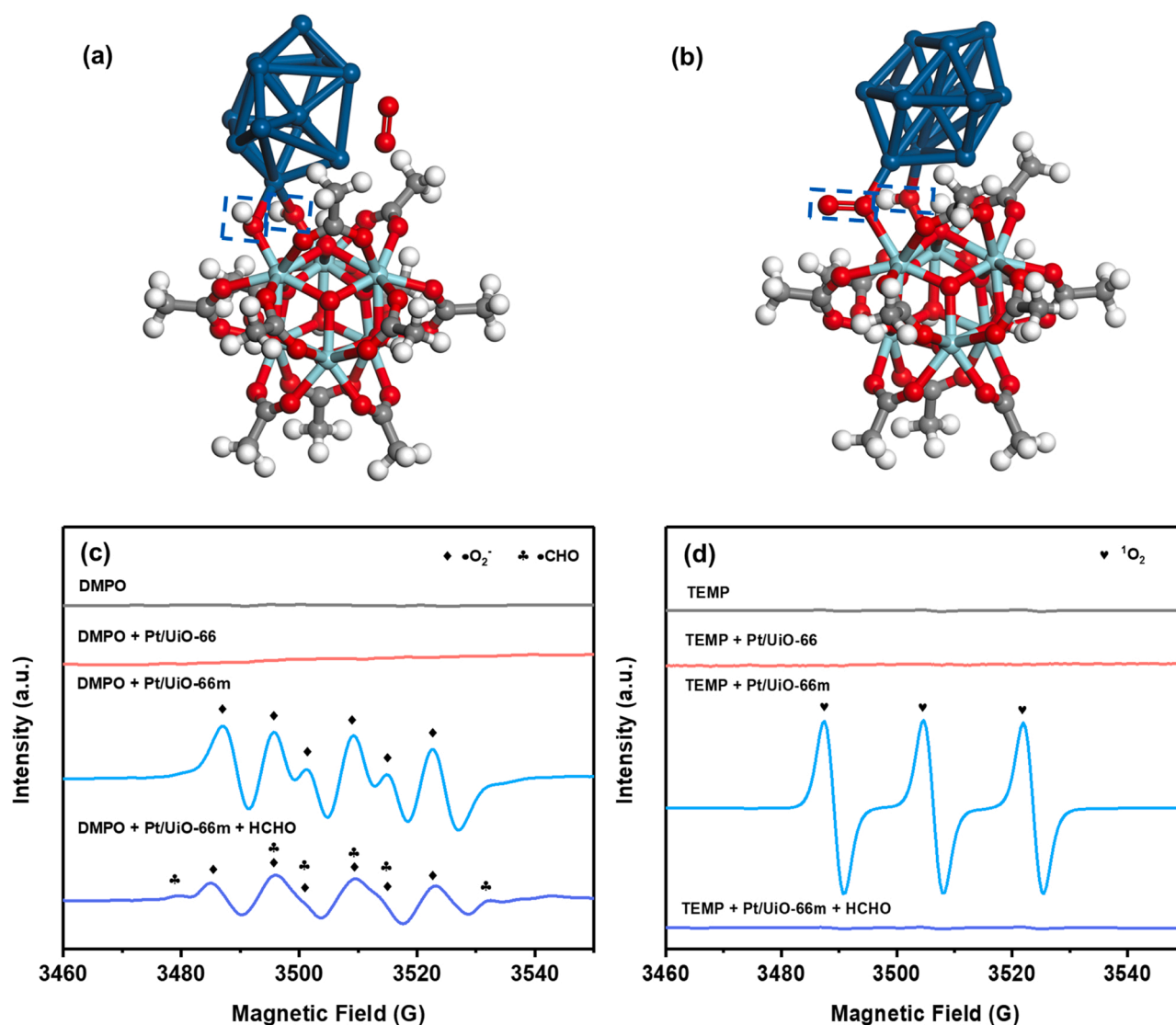


Fig. 6. (a) The most favorable configuration of the O₂ adsorbed on the surface of Pt on Pt₁₃/UiO-66m (–OH/–OH). (b) The configuration of the monodentate O₂ adsorbed at Zr-CUSs–Pt sites (model 1). Spin-trapping EPR spectra of O₂-derived ROSS over Pt/UiO-66 and Pt/UiO-66m: (c) DMPO in methanol (superoxide radicals) suspension and (d) TEMP in aqueous solution (singlet oxygen) at 25 °C.

the characteristic peaks of $\text{DMPO}\bullet\text{O}_2^-$ adduct with relative intensity of 1:2:2:1 (Fig. 6c). Afterward, the unpaired electron of $\bullet\text{O}_2^-$ may return to neighboring $\text{Pt}^{\delta+}$, resulting in the formation of $^1\text{O}_2$ [22], as identified by characteristic peaks of TEMPO with the 1:1:1 triplet signal (Fig. 6d). In the presence of HCHO, the intensity of $\text{DMPO}\bullet\text{O}_2^-$ adduct and TEMPO peaks were significantly decreased, implying that the HCHO oxidation would occur by ROS-initiated reactions. Moreover, the radical intermediates ($\bullet\text{CHO}$) was recorded (Fig. 6c), confirming that HCHO can be oxidized to $\bullet\text{CHO}$ by $\bullet\text{O}_2^-$ by radical propagation.

3.4. HCHO oxidation activity and mechanism

The performance of UiO-66, UiO-66m, Pt/UiO-66, and Pt/UiO-66m catalysts for HCHO removal and oxidation were both evaluated by static activity test and dynamic activity test at room temperature. In the box reactor, UiO-66 and UiO-66m catalysts exhibited only 28.5% and 30.0% removal efficiency in 60 min but the figure for mineralization remained virtually unchanged, because they cannot effectively activate molecular oxygen and no catalytic oxidation proceeded (Fig. 7a, b). By contrast, after loading Pt NPs, the molecular oxygen can be activated and HCHO oxidation activities were intensely enhanced. In the case of Pt/UiO-66, 80.0% of HCHO can be removed in 60 min and partially (72.5%) oxidized to H_2O and CO_2 . Pt/UiO-66m exhibited much higher

HCHO oxidation activity than Pt/UiO-66, with excellent HCHO removal efficiency (97.7%) and mineralization efficiency (98.6%) within 60 min. Typically, Pt species on Pt/UiO-66 and Pt/UiO-66m can activate the molecular oxygen into atomic oxygen, which could oxidize HCHO and intermediate products to CO_2 and H_2O . Strikingly, another molecular oxygen activation pathway occurred at the Zr-CUSs-Pt active sites of Pt/UiO-66m and generated mobile $\bullet\text{O}_2^-$ and $^1\text{O}_2$ that oxidize HCHO more efficiently, leading to much higher HCHO removal and mineralization efficiency. The TOF of Pt/UiO-66m ($2.52 \times 10^{-1} \text{ s}^{-1}$) is also higher than that of Pt/UiO-66 ($1.17 \times 10^{-1} \text{ s}^{-1}$) and most Pt-based catalysts reported in the literature, indicating the superior intrinsic activity of the Pt/UiO-66m catalyst (Table 1, Table S4, and Fig. S14). At different initial concentrations (around 210 ppm and 7.5 ppm), the Pt/UiO-66m still exhibited outstanding removal efficiency (above 98.0% and 90.0% within 60 min) (Fig. S13). We also evaluated the dynamic catalytic activity of Pt/UiO-66m in a continuous-flow system at room temperature to assess its effectiveness in mitigating long-term indoor HCHO emissions. When the Pt/UiO-66m catalyst was exposed to a gas flow of 8 ppm HCHO, 21% O_2 , and 30% RH balanced by nitrogen, the HCHO removal and mineralization efficiency were above 98.0% in 24 h (Fig. S15a, b). The superior HCHO catalytic oxidation performance of the Pt/UiO-66m is related to the cooperative effects of the strong electronic metal support interactions at Zr-CUSs-Pt active centers and the acid-basic

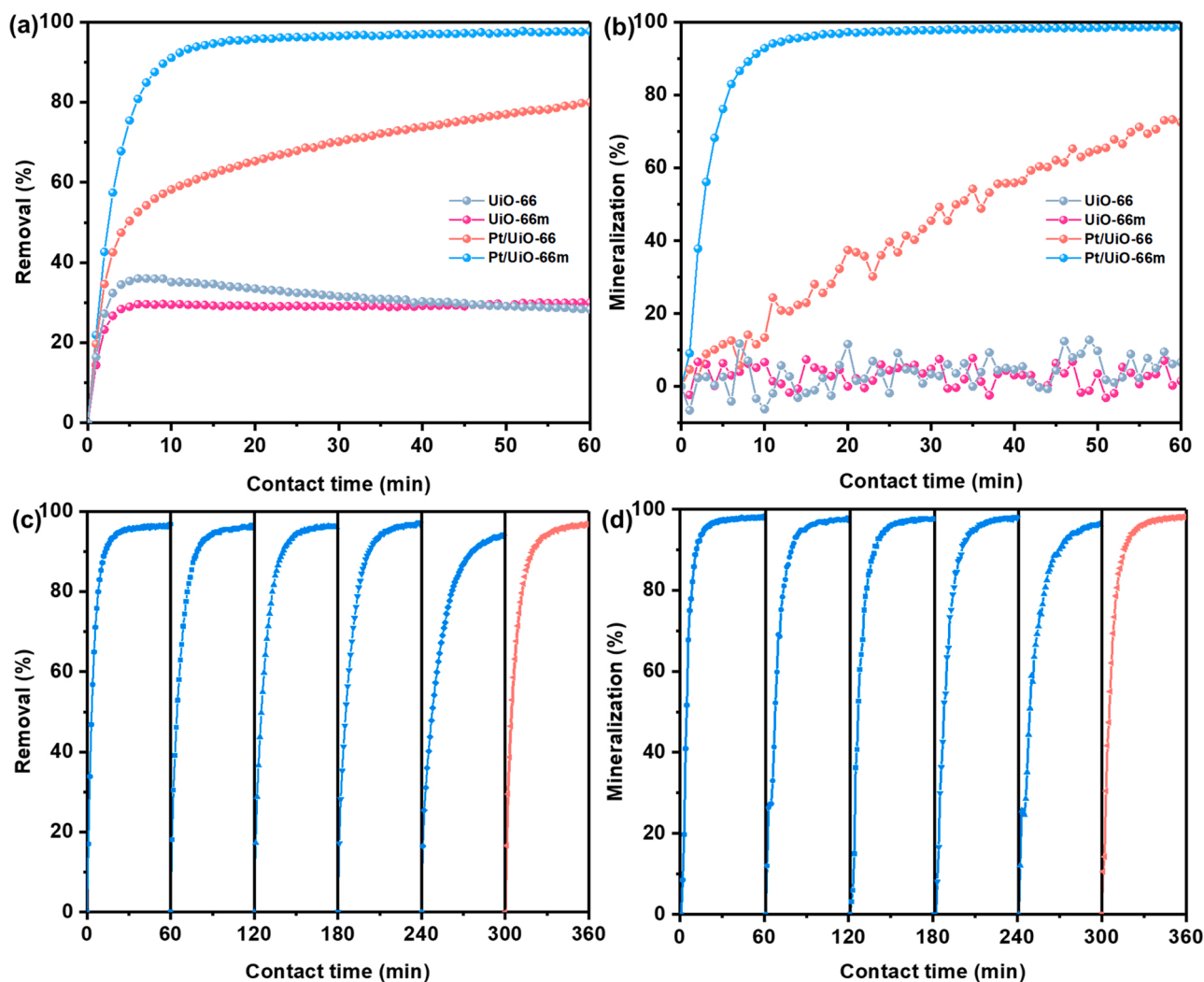


Fig. 7. (a) HCHO removal efficiency, (b) mineralization efficiency of UiO-66, UiO-66m, Pt/UiO-66, and Pt/UiO-66m in a box reactor. (c) HCHO removal efficiency and (d) mineralization efficiency of Pt/UiO-66m sample in recycling test (blue dotted line) in the box reactor. After the fifth test, the samples were washed with deionized water three times and dried at 60 °C (HCHO = 115 ± 5 ppm, RH = $30 \pm 3\%$).

catalysis. Without strong EMSI, Pt/Uio-66 exhibit lower acid/basic density and weaker activation of molecular oxygen, resulting in inferior HCHO removal performances. In practical conditions, the cycling stability of Pt/Uio-66m is also of great importance. The stability test was first carried out by a series of repeated experiments with analogous initial HCHO concentration in the box reactor (Fig. 7c, d). A consistently high HCHO removal efficiency of over 94.2% and mineralization efficiency of over 96.4% were maintained over five consecutive runs (5 h) with the Pt/Uio-66m sample, with a reduction in HCHO removal efficiency of less than 4%. The slight decline in removal efficiency is mainly due to the accumulation of water-soluble intermediates (formate species and/or carbonate species). After rinsing with deionized water, the Pt/Uio-66m can be regenerated as fresh catalysts. In the continuous-flow system, when the Pt/Uio-66m catalyst was exposed to a gas flow of 115 ppm HCHO, 21% O₂, and 30% RH balanced by nitrogen, the HCHO removal and mineralization efficiency was above 94% in 12 h (Fig. S15c, d). The comparison of the PXRD patterns FTIR spectra and XPS survey spectra of the fresh and the used Pt/Uio-66m catalyst (Fig. S16a-d) indicates that the crystallinity and basic structure of the catalyst are retained, demonstrating the high stability of the catalyst. Moreover, the chemical states of Pt species were basically remained, with the percentage of Pt^{δ+} slightly increasing from 39.5% (fresh) to 41.5% (used), indicating the superior stability of Pt which is influenced by the EMSI effect.

To investigate the generality of the O₂ activation strategy by loading noble metal NPs in defective UiO-66m, Pt has been replaced by another noble metal (Pd) to synthesize Pd/Uio-66m. As shown in Fig. S17, superoxide radicals (•O₂⁻) and singlet oxygen (¹O₂) were also recorded over Pd/Uio-66m. Compared to lower removal efficiency (69.0%) and mineralization efficiency (54.7%) on Pd/Uio-66, Pd/Uio-66m showed significant HCHO removal efficiency (91.1%) and mineralization efficiency (92.5%) in 60 min (Fig. S18). This result suggests that in the M/Uio-66m system, Pt NPs may have a superior O₂ activation ability than Pd NPs.

To explore the reaction mechanism, the adsorbed reaction intermediates of the HCHO oxidation process over Pt/Uio-66 and M/Uio-66m (M = Pt, Pd) in a flow of HCHO (115 ppm) in synthetic air were characterized by *in situ* DRIFTS at room temperature (Fig. 8a, Fig. S19a). Corresponding wavenumbers of the adsorbed reaction intermediates were listed in Table 2. After being exposed to a flow of HCHO + N₂ + O₂ + H₂O, the bands ascribed to the surface hydroxyl group (3672 cm⁻¹), adsorbed H₂O (1640, 3413, 3448, and 3571 cm⁻¹), adsorbed HCHO

Table 2

Wavenumbers (cm⁻¹) of the intermediates that formed during HCHO oxidation on Pt/Uio-66, Pt/Uio-66m, and Pd/Uio-66m.

Pt/Uio-66	Pt/Uio-66m	Pd/Uio-66m	Assignment	Reference
3672	3672	3672	μ ₃ -OH, terminal -OH and -OH ₂	[39]
	3729, 3780		Zr-OH	[53]
3571	3413, 3445, 3473	3448	ν(OH) of adsorbed H ₂ O	[44]
1640	1640	1640	δ(OH) of adsorbed H ₂ O	[5]
	1724, 1732	1724	ν(CO) of HCHO	[44]
1261	1261, 1273	1260	ω(CH ₂) of HCHO	[45]
1032	1032	1032	ν(CO) of DOM	[46]
1300	1300	1296	τ(CH ₂) of DOM	[47]
1406, 1404	1406, 1402	1404	ω(CH ₂) of DOM	[48]
1481	1481	1481	δ(CH ₂) of DOM	[48]
1366, 1362	1366	1365	ν _s (OCO) of bidentate formate species	[5]
1601, 1617	1596, 1599, 1601	1601	ν _{as} (OCO) of monodentate formate species	[5]
1543	1543	1543	ν _{as} (OCO) of bidentate formate species	[5]
	2908, 2886	2886	ν(CH) of formate species	[49]
	2977	2953	ν _a (OCO) + δ(CH) of formate species	[50]
1666	1660, 1666, 1670	1670	ν _s (CO) of carbonate species	[51]
	2025		linearly adsorbed CO	[38]

(1260–1261 and 1724 cm⁻¹), dioxymethylene (DOM, 1032, 1296–1300, 1406, and 1481 cm⁻¹) and formate species (1365–1366, 1543, 1601, 2886–2908, and 2953–2977 cm⁻¹), carbonate species (1666–1670 cm⁻¹) were detected [5,39,44–51]. HCHO, DOM, formate species, and carbonate species appeared both on Pt/Uio-66 and M/Uio-66m, indicating that DOM, formate species, and carbonate species are the dominant intermediates in the reaction process. In comparison to Pt/Uio-66, the negative peak at 3672 cm⁻¹ (the -OH groups from the adsorption and activation of water) are more pronounced on Pt/Uio-66m, and the intensity of DOM and formate species on Pt/Uio-66m increased more quickly and was stronger when equilibrium was reached, indicating the superior catalytic performance of Pt/Uio-66m. It is suggested that the conversion of formate species is a rate-determining step and with the accumulation of formate species, the active sites of catalysts may be occupied, resulting in the deactivation of

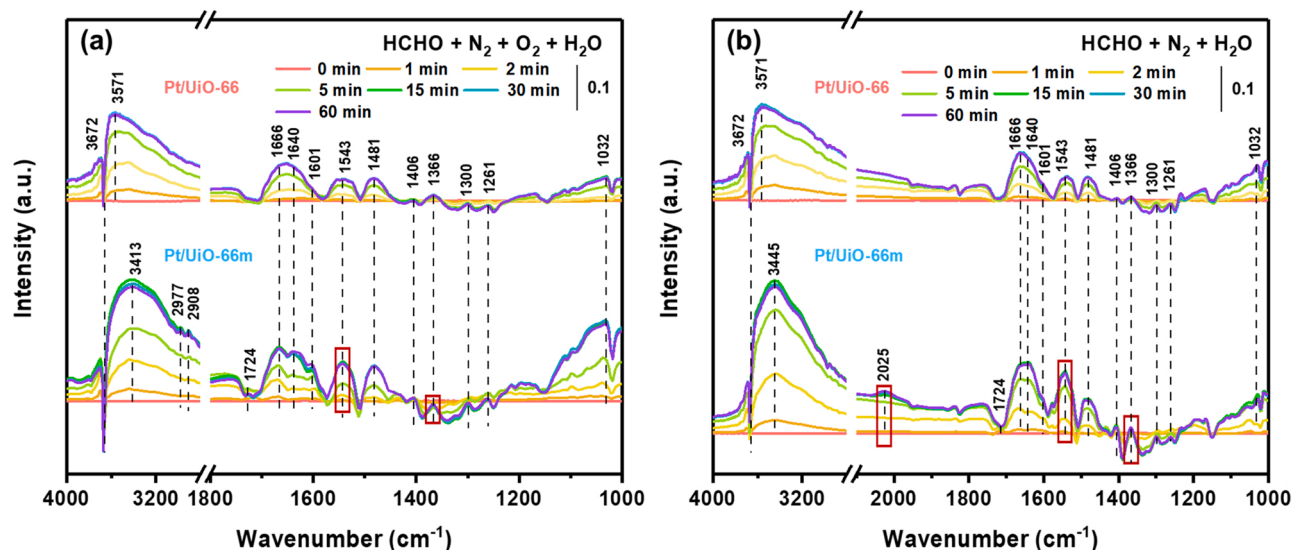


Fig. 8. *In situ* DRIFTS spectra of Pt/Uio-66 and Pt/Uio-66m samples exposed to the flow of (a) HCHO + N₂ + O₂ + H₂O and (b) HCHO + N₂ + H₂O at room temperature (HCHO = 115 ppm, RH = 30%).

the catalysts [52]. For Pt/UiO-66m, the intensity of carbonate species (1666 cm^{-1}) was also more pronounced, suggesting a quicker formation of carbonate species due to the accelerated conversion of formaldehyde through ROS-initiated pathways [44].

To explore the effect of O_2 and H_2O in the HCHO oxidation process, comparative experiments were performed on Pt/UiO-66 and Pt/UiO-66m (Fig. 8b). Similarly, in the flow of $\text{HCHO} + \text{N}_2 + \text{H}_2\text{O}$, the bands ascribed to surface hydroxyl group (3672 cm^{-1}), adsorbed H_2O (1640 , 3445 , and 3571 cm^{-1}), adsorbed HCHO (1261 and 1724 cm^{-1}), DOM (1032 , 1300 , 1406 , and 1481 cm^{-1}) and formate species (1366 , 1543 , 1601 , 2908 , and 2977 cm^{-1}), carbonate species (1666 cm^{-1}) were detected. Notably, for Pt/UiO-66m, the intensity of formate species (1366 and 1543 cm^{-1}) was stronger than in the presence of O_2 . CO (2025 cm^{-1}) was observed after 5 min, generated from the decomposition of formate species [9]. These results demonstrate that the activation of O_2 plays a crucial role in the oxidation of formate species. The HCHO removal performance experiment was usually carried out in the air, containing 21% O_2 . In this case, almost no CO was detected over Pt/UiO-66m (Fig. S19b). For Pt/UiO-66, the intensity of characteristic peaks did not change a lot whether O_2 was present or not, suggesting that the conversion of HCHO into DOM and formate species is faster than the oxidation of formate species over Pt/UiO-66.

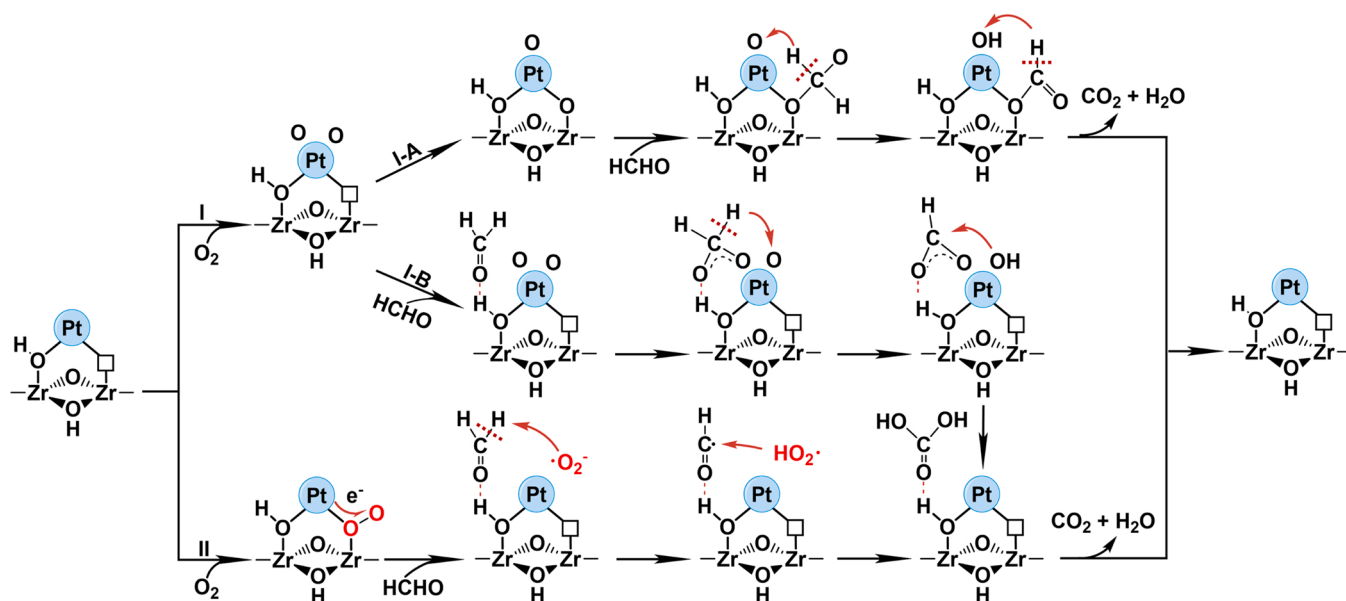
In the flow of $\text{HCHO} + \text{N}_2 + \text{O}_2$ (Fig. S20), HCHO (1732 and 1273 cm^{-1}) is adsorbed and transformed into monodentate formate species (1596 cm^{-1}) with consumption of surface hydroxyl group (3672 cm^{-1}) on Pt/UiO-66m and after adding the H_2O to the flow, the peaks of adsorbed H_2O (1640 and 3473 cm^{-1}), DOM (1032 , 1300 , 1406 , and 1481 cm^{-1}), formate species (1366 , 1543 , and 1601 cm^{-1}), and carbonate species (1660 cm^{-1}) were recorded. This result demonstrates that the activation of water is crucial to initiate the conversion of HCHO into DOM as well as formate species through the acid-base catalysis process. The conclusion can also be proved from the performance test with different RH (Fig. S21). In the wide RH range of 5–75%, the high HCHO oxidation activity of Pt/UiO-66m persists, while in ultralow RH (RH = 5% or 0% in dry air), the removal efficiency decreased slightly and the conversion rate of HCHO became much slower.

In the flow of $\text{HCHO} + \text{N}_2$ (Fig. S22), HCHO (1724 and 1261 cm^{-1}) can be transformed into DOM (1032 , 1300 , 1406 , and 1481 cm^{-1}), formate species (1366 , 1543 , and 1601 – 1617 cm^{-1}) with the consumption of surface hydroxyl group (3672 cm^{-1}) on Pt/UiO-66 and Pt/UiO-66m, while the intensity of these intermediates was weaker than in

the presence of H_2O and O_2 . Notably, for Pt/UiO-66m, the negative bands at 3729 cm^{-1} and 3780 cm^{-1} attributed to Zr-OH were observed, demonstrating that different kinds of $-\text{OH}$ was consumed because of the increasing concentration of missing linker/cluster defects [53]. The intensity of carbonate species (1666 cm^{-1}) and water (1640 cm^{-1}) increased at the initial 5 min and then decreased, indicating that the active oxygen species can remain on the Pt/UiO-66 m.

Based on the above studies, the possible HCHO oxidation pathways on Pt/UiO-66 and M/UiO-66m ($\text{M} = \text{Pt}, \text{Pd}$) are proposed and illustrated in Scheme 2, using Pt/UiO-66m as an example. Before being exposed to the gaseous HCHO molecule, H_2O (4 \AA) is adsorbed and activated into $-\text{OH}$ through the open window (6 \AA), and O_2 (3.46 \AA) is adsorbed on the surface of Pt NPs or at the Zr-CUSs–Pt sites. Generally, O_2 can dissociate into atomic oxygen on the surface of Pt species (path I). In this case, two branches may occur. In path I-A, atomic oxygen can migrate to the Zr-CUSs–Pt site, serving as a Brønsted basic site. HCHO is adsorbed at this site, transformed into DOM, and further deprotonated by atomic oxygen, forming monodentate formate species and active OH. Finally, formate species are oxidized into CO_2 and H_2O by active OH. In path I-B, HCHO can be adsorbed on the bridging $-\text{OH}$. Subsequently, the atomic oxygen attacks the electrophilic carbon, resulting in the conversion of HCHO into DOM. This is then further deprotonated by another atomic oxygen, forming monodentate formate species and active OH. Finally, formate species are oxidized into the H_2CO_3 , which finally decomposes into free CO_2 and H_2O . Path II is a ROS-initiated advanced oxidation pathway, in which O_2 can be activated into ROS at the Zr-CUSs–Pt sites and fewer intermediates are accumulated. Firstly, O_2 is activated into $\bullet\text{O}_2^-$. Then, the adsorbed HCHO is transformed into $\bullet\text{CHO}$ and H_2CO_3 sequentially because of ROS's significant mobility and reactivity. Finally, the H_2CO_3 decomposes into CO_2 and H_2O and releases from the catalyst.

Notably, during the HCHO oxidation processes, the surface acidity/basicity enhanced by H_2O adsorption and activation on Pt/UiO-66m is also crucial. Although the HCHO oxidation is dominated by O_2 activation, the resulting active atomic oxygen and ROS is mainly bound to the catalysts surface. In this regard, the promoted HCHO adsorption and activation at basic sites, close to the O_2 activation sites, increase their collision possibility and promote the oxidation reaction efficiency. On the other hand, the HCHO derived final CO_2 products may be existing as H_2CO_3 , HCO_3^- and/or CO_3^{2-} , which may be accumulated on the catalyst surface and occupying active sites. The surface acidic sites would accelerate the decomposition of those carbonate species into free CO_2



Scheme 2. Schematic illustration of the catalytic HCHO oxidation mechanism over Pt/UiO-66m samples (squares represent Zr-CUSs).

molecules escaping from catalyst surface, which is crucial for catalyst regeneration and recycling.

4. Conclusion

The abundant Zr-CUSs in UiO-66m favored for uniform anchoring noble metal catalyst with strong EMSI and introduced a unique multifunctional Zr-CUSs-M active centers. As a result, the strength and density of acidic/basic sites were enhanced by H₂O adsorption and activated at those Zr-CUSs-M sites. Moreover, those Zr-CUSs-M sites triggered another molecular oxygen activation pathway and generated mobile ROSs, including $\bullet\text{O}_2^-$ and $^1\text{O}_2$, which in turn initiated advanced HCHO oxidation pathway. Owing to the synergistic effect of H₂O and O₂ activation, HCHO can be converted into CO₂ and H₂O with superior efficiency and durability. This study will offer a new perspective for activating molecular O₂ and exploiting advanced RTCO catalysts. The presented Pt/UiO-66m with unique Zr-CUSs-Pt active sites is a promising RTCO catalyst with high catalytic activity and long-term stability, even superior to the currently available benchmark Pt/TiO₂ catalyst (Fig. S23), offering potential applications for fast indoor air purification at ambient temperature.

CRediT authorship contribution statement

Yifan Zhuo: Investigation, Writing – original draft. **Xiuling Guo:** Investigation. **Wei Cai:** Assist in experimental tests. **Tao Shao:** Methodology. **Dehua Xia:** Supervision. **Chuanhao Li:** Supervision. **Shengwei Liu:** Conceptualization, Supervision, Writing – review & editing, Funding acquisition.

Declaration of Competing Interest

The authors declare that they have no known competing financial interests or personal relationships that could have appeared to influence the work reported in this paper.

Data Availability

Data will be made available on request.

Acknowledgements

This work was financially supported by the National Natural Science Foundation of China (51872341), the Tip-top Scientific and Technical Innovative Youth Talents of Guangdong Special Support Program (2019TQ05L196), and the Science and Technology Planning Project of Guangdong Province (2021A1515010147).

Appendix A. Supporting information

Supplementary data associated with this article can be found in the online version at [doi:10.1016/j.apcatb.2023.122789](https://doi.org/10.1016/j.apcatb.2023.122789).

References

- C. He, J. Cheng, X. Zhang, M. Douthwaite, S. Pattison, Z.P. Hao, Recent advances in the catalytic oxidation of volatile organic compounds: a review based on pollutant sorts and sources, *Chem. Rev.* 119 (2019) 4471–4568, <https://doi.org/10.1021/acs.chemrev.8b00408>.
- J.W. Ye, Y. Yu, J.J. Fan, B. Cheng, J.G. Yu, W.K. Ho, Room-temperature formaldehyde catalytic decomposition, *Environ. Sci. Nano* 7 (2020) 3655–3709, <https://doi.org/10.1039/d0en00831a>.
- K. Vellingiri, K. Vikrant, V. Kumar, K.H. Kim, Advances in thermocatalytic and photocatalytic techniques for the room/low temperature oxidative removal of formaldehyde in air, *Chem. Eng. J.* 399 (2020), 125759, <https://doi.org/10.1016/j.cej.2020.125759>.
- J.B. Li, X. Wu, S.W. Liu, Fluorinated TiO₂ hollow photocatalysts for photocatalytic applications, *Acta Phys. -Chim. Sin.* 37 (2021), 2009038, <https://doi.org/10.3866/pku.Whxb202009038>.
- J.H. Guo, C.X. Lin, C.J. Jiang, P.Y. Zhang, Review on noble metal-based catalysts for formaldehyde oxidation at room temperature, *Appl. Surf. Sci.* 475 (2019) 237–255, <https://doi.org/10.1016/j.apsusc.2018.12.238>.
- R.Y. Chen, Z.Z. Sun, C. Hardacre, X.F. Tang, Z.M. Liu, The current status of research on the catalytic oxidation of formaldehyde, *Catal. Rev.* (2022) 1–56, <https://doi.org/10.1080/01614940.2022.2107785>.
- M.M. Huang, Y.X. Li, M.W. Li, J. Zhao, Y.Q. Zhu, C.Y. Wang, V.K. Sharma, Active site-directed tandem catalysis on single platinum nanoparticles for efficient and stable oxidation of formaldehyde at room temperature, *Environ. Sci. Technol.* 53 (2019) 3610–3619, <https://doi.org/10.1021/acs.est.9b01176>.
- J.Y. Ding, Y.J. Yang, J. Liu, Z. Wang, Catalytic reaction mechanism of formaldehyde oxidation by oxygen species over Pt/TiO₂ catalyst, *Chemosphere* 248 (2020), 125980, <https://doi.org/10.1016/j.chemosphere.2020.125980>.
- Z.L. Zhang, G.Z. He, Y.B. Li, C.B. Zhang, J.Z. Ma, H. He, Effect of hydroxyl groups on metal anchoring and formaldehyde oxidation performance of Pt/Al₂O₃, *Environ. Sci. Technol.* 56 (2022) 10916–10924, <https://doi.org/10.1021/acs.est.2c01278>.
- U.J. Etim, P. Bai, O.M. Gazit, Z. Zhong, Low-temperature heterogeneous oxidation catalysis and molecular oxygen activation, *Catal. Rev.* (2021) 1–187, <https://doi.org/10.1080/01614940.2021.1919044>.
- S.P. Li, C.I. Ezugwu, S.P. Zhang, Y. Xiong, S.W. Liu, Co-doped MgAl-LDHs nanosheets supported Au nanoparticles for complete catalytic oxidation of HCHO at room temperature, *Appl. Surf. Sci.* 487 (2019) 260–271, <https://doi.org/10.1016/j.apsusc.2019.05.083>.
- C.Y. Wang, Y.B. Li, C.B. Zhang, X.Y. Chen, C.L. Liu, W.Z. Weng, W.P. Shan, H. He, A simple strategy to improve Pd dispersion and enhance Pd/TiO₂ catalytic activity for formaldehyde oxidation: the roles of surface defects, *Appl. Catal. B* 282 (2021), 119540, <https://doi.org/10.1016/j.apcatb.2020.119540>.
- H.Y. Tan, J. Wang, S.Z. Yu, K.B. Zhou, Support morphology-dependent catalytic activity of Pd/CeO₂ for formaldehyde oxidation, *Environ. Sci. Technol.* 49 (2015) 8675–8682, <https://doi.org/10.1021/acs.est.5b01264>.
- T.W. van Deelen, C.H. Mejia, K.P. de Jong, Control of metal-support interactions in heterogeneous catalysts to enhance activity and selectivity, *Nat. Catal.* 2 (2019) 955–970, <https://doi.org/10.1038/s41929-019-0364-x>.
- A. Bruix, J.A. Rodriguez, P.J. Ramirez, S.D. Senanayake, J. Evans, J.B. Park, D. Stacchiola, P. Liu, J. Hrbeek, F. Illas, A new type of strong metal-support interaction and the production of H₂ through the transformation of water on Pt/CeO₂(111) and Pt/CeO_x/TiO₂(110) catalysts, *J. Am. Chem. Soc.* 134 (2012) 8968–8974, <https://doi.org/10.1021/ja302070k>.
- J.R. Yang, W.H. Li, D.S. Wang, Y.D. Li, Electronic metal-support interaction of single-atom catalysts and applications in electrocatalysis, *Adv. Mater.* 32 (2020), 2003300, <https://doi.org/10.1002/adma.202003300>.
- Z.Y. Jiang, M.J. Tian, M.Z. Jing, S.N. Chai, Y.F. Jian, C.W. Chen, M. Douthwaite, L. R. Zheng, M.D. Ma, W.Y. Song, J. Liu, J.G. Yu, C. He, Modulating the electronic metal-support interactions in single-atom Pt₁-CuO catalyst for boosting acetone oxidation, *Angew. Chem. Int. Ed.* 61 (2022), e202200763, <https://doi.org/10.1002/anie.202200763>.
- L. Ma, X.Y. Chen, J.H. Li, H.Z. Chang, J.W. Schwank, Electronic metal-support interactions in Pt/FeO_x nanospheres for CO oxidation, *Catal. Today* 355 (2020) 539–546, <https://doi.org/10.1016/j.cattod.2019.06.055>.
- M.L. Xiao, L.Q. Gao, Y. Wang, X. Wang, J.B. Zhu, Z. Jin, C.P. Liu, H.Q. Chen, G. R. Li, J.J. Ge, Q.G. He, Z.J. Wu, Z.W. Chen, W. Xing, Engineering energy level of metal center: Ru single-atom site for efficient and durable oxygen reduction catalysis, *J. Am. Chem. Soc.* 141 (2019) 19800–19806, <https://doi.org/10.1021/jacs.9b09234>.
- Y.C. Yao, S.L. Hu, W.X. Chen, Z.Q. Huang, W.C. Wei, T. Yao, R.R. Liu, K.T. Zang, X. Q. Wang, G. Wu, W.J. Yuan, T.W. Yuan, B.Q. Zhu, W. Liu, Z.J. Li, D.S. He, Z.G. Xue, Y. Wang, X.S. Zheng, J.C. Dong, C.R. Chang, Y.X. Chen, X. Hong, J. Luo, S.Q. Wei, W.X. Li, P. Strasser, Y.E. Wu, Y.D. Li, Engineering the electronic structure of single atom Ru sites via compressive strain boosts acidic water oxidation electrocatalysis, *Nat. Catal.* 2 (2019) 304–313, <https://doi.org/10.1038/s41929-019-0246-2>.
- M.J. Wu, G.X. Zhang, W.C. Wang, H.M. Yang, D. Rawach, M.J. Chen, S.H. Sun, Electronic metal support interaction modulation of single-atom electrocatalysts for rechargeable zinc-air batteries, *Small Methods* 6 (2022), 2100947, <https://doi.org/10.1002/smt.202100947>.
- Y. Yin, Y. Ren, J.H. Lu, W.M. Zhang, C. Shan, M. Hua, L. Lv, B.C. Pan, The nature and catalytic reactivity of UiO-66 supported Fe₃O₄ nanoparticles provide new insights into Fe-Zr dual active centers in Fenton-like reactions, *Appl. Catal. B* 286 (2021), 119943, <https://doi.org/10.1016/j.apcatb.2021.119943>.
- F. Ahmadijokani, H. Molavi, M. Rezakazemi, S. Tajahmadi, A. Bahi, F. Ko, T. M. Aminabhavi, J.R. Li, M. Arjmand, UiO-66 metal-organic frameworks in water treatment: a critical review, *Prog. Mater. Sci.* 125 (2022), 100904, <https://doi.org/10.1016/j.pmatsci.2021.100904>.
- C.I. Ezugwu, S.P. Zhang, S.P. Li, S.R. Shi, C.H. Li, F. Verpoort, J.G. Yu, S.W. Liu, Efficient transformative HCHO capture by defective NH₂-UiO-66(Zr) at room temperature, *Environ. Sci. Nano* 6 (2019) 2931–2936, <https://doi.org/10.1039/c9en00871c>.
- J.H. Cavka, S. Jakobsen, U. Olsbye, N. Guillou, C. Lamberti, S. Bordiga, K. P. Lillerud, A new zirconium inorganic building brick forming metal organic frameworks with exceptional stability, *J. Am. Chem. Soc.* 130 (2008) 13850–13851, <https://doi.org/10.1021/ja8057953>.
- X.T. Hou, J.C. Wang, B. Mousavi, N. Klonkiliang, S. Chaemchuen, Strategies for induced defects in metal-organic frameworks for enhancing adsorption and catalytic performance, *Dalton Trans.* 51 (2022) 8133–8159, <https://doi.org/10.1039/d2dt01030e>.

- [27] J.J. Li, Q.Q. Guan, H. Wu, W. Liu, Y. Lin, Z.H. Sun, X.X. Ye, X.S. Zheng, H.B. Pan, J. F. Zhu, S. Chen, W.H. Zhang, S.Q. Wei, J.L. Lu, Highly active and stable metal single-atom catalysts achieved by strong electronic metal-support interactions, *J. Am. Chem. Soc.* 141 (2019) 14515–14519, <https://doi.org/10.1021/jacs.9b06482>.
- [28] G.C. Shearer, S. Chavan, S. Bordiga, S. Svelle, U. Olsbye, K.P. Lillerud, Defect engineering: tuning the porosity and composition of the metal-organic framework UiO-66 via modulated synthesis, *Chem. Mater.* 28 (2016) 3749–3761, <https://doi.org/10.1021/acs.chemmater.6b00602>.
- [29] X.D. Zhang, X.T. Lv, X.Y. Shi, Y. Yang, Y.Q. Yang, Enhanced hydrophobic UiO-66 (University of Oslo 66) metal-organic framework with high capacity and selectivity for toluene capture from high humid air, *J. Colloid Interface Sci.* 539 (2019) 152–160, <https://doi.org/10.1016/j.jcis.2018.12.056>.
- [30] H. Li, H.J. Chu, X.L. Ma, G.R. Wang, F.S. Liu, M. Guo, W.P. Lu, S.J. Zhou, M.Z. Yu, Efficient heterogeneous acid synthesis and stability enhancement of UiO-66 impregnated with ammonium sulfate for biodiesel production, *Chem. Eng. J.* 408 (2021), 127277, <https://doi.org/10.1016/j.cej.2020.127277>.
- [31] K. Chakarova, I. Strauss, M. Mihaylov, N. Drenchev, K. Hadjiivanov, Evolution of acid and basic sites in UiO-66 and UiO-66-NH₂ metal-organic frameworks: FTIR study by probe molecules, *Microporous Mesoporous Mater.* 281 (2019) 110–122, <https://doi.org/10.1016/j.micromeso.2019.03.006>.
- [32] R. Thur, N. Van Velthoven, V. Lemmens, M. Bastin, S. Smolders, D. De Vos, I.F. J. Vankelecom, Modulator-mediated functionalization of MOF-808 as a platform tool to create high-performance mixed-matrix membranes, *ACS Appl. Mater. Interfaces* 11 (2019) 44792–44801, <https://doi.org/10.1021/acsami.9b19774>.
- [33] J.W.O. Tam, I.M. Klotz, Protonation of amides by trifluoroacetic acid: infrared and nuclear magnetic resonance studies, *Spectrochim. Acta, Part A* 29 (1973) 633–644, [https://doi.org/10.1016/0584-8539\(73\)80093-5](https://doi.org/10.1016/0584-8539(73)80093-5).
- [34] F.G. Cirujano, F. Xamena, Tuning the catalytic properties of UiO-66 metal-organic frameworks: from Lewis to defect-induced Brønsted acidity, *J. Phys. Chem. Lett.* 11 (2020) 4879–4890, <https://doi.org/10.1021/acs.jpclett.0c00984>.
- [35] L.N. Zhang, Q.Q. Bao, B.J. Zhang, Y.B. Zhang, S.L. Wan, S. Wang, J.D. Lin, H. F. Xiong, D.H. Mei, Y. Wang, Distinct role of surface hydroxyls in single-atom Pt₁/CeO₂ catalyst for room-temperature formaldehyde oxidation: acid-base versus redox, *JACS Au* 2 (2022) 1651–1660, <https://doi.org/10.1021/jacsau.2c00215>.
- [36] G. Ye, H.L. Wang, X.Y. Zeng, L. Wang, J. Wang, Defect-rich bimetallic UiO-66(Hf-Zr): solvent-free rapid synthesis and robust ambient-temperature oxidative desulfurization performance, *Appl. Catal. B* 299 (2021), 120659, <https://doi.org/10.1016/j.apcatb.2021.120659>.
- [37] J.W. Ye, M.H. Zhou, Y. Le, B. Cheng, J.G. Yu, Three-dimensional carbon foam supported MnO₂/Pt for rapid capture and catalytic oxidation of formaldehyde at room temperature, *Appl. Catal. B* 267 (2020), 118689, <https://doi.org/10.1016/j.apcatb.2020.118689>.
- [38] H.L. Tang, Y. Su, Y.L. Guo, L.L. Zhang, T.B. Li, K.T. Zang, F. Liu, L. Li, J. Luo, B. T. Qiao, J.H. Wang, Oxidative strong metal-support interactions (OMSI) of supported platinum-group metal catalysts, *Chem. Sci.* 9 (2018) 6679–6684, <https://doi.org/10.1039/c8sc01392f>.
- [39] J. Sui, H. Liu, S. Hu, K. Sun, G. Wan, H. Zhou, X. Zheng, H.L. Jiang, A general strategy to immobilize single-atom catalysts in metal-organic frameworks for enhanced photocatalysis, *Adv. Mater.* 34 (2022), 2109203, <https://doi.org/10.1002/adma.202109203>.
- [40] C.Y. Wang, Y.B. Li, L.R. Zheng, C.B. Zhang, Y. Wang, W.P. Shan, F.D. Liu, H. He, A nonoxide catalyst system study: alkali metal-promoted Pt/AC catalyst for formaldehyde oxidation at ambient temperature, *ACS Catal.* 11 (2021) 456–465, <https://doi.org/10.1021/acscatal.0c03196>.
- [41] J.L. Wang, X.F. Shi, L.W. Chen, H.Y. Li, M.Q. Mao, G.Y. Zhang, H. Yi, M.L. Fu, D. Q. Ye, J.L. Wu, Enhanced performance of low Pt loading amount on Pt-CeO₂ catalysts prepared by adsorption method for catalytic ozonation of toluene, *Appl. Catal. A* 625 (2021), 118342, <https://doi.org/10.1016/j.apcata.2021.118342>.
- [42] W.J. Bao, H.X. Chen, H. Wang, R.D. Zhang, Y. Wei, L.R. Zheng, Pt nanoparticles supported on N/Ce-doped activated carbon for the catalytic oxidation of formaldehyde at room temperature, *ACS Appl. Nano Mater.* 3 (2020) 2614–2624, <https://doi.org/10.1021/acsnanm.0c00005>.
- [43] M.M. Montemore, M.A. van Spronsen, R.J. Madix, C.M. Friend, O₂ activation by metal surfaces: implications for bonding and reactivity on heterogeneous catalysts, *Chem. Rev.* 118 (2018) 2816–2862, <https://doi.org/10.1021/acs.chemrev.7b00217>.
- [44] S.P. Zhang, Y.F. Zhuo, C.I. Ezugwu, C.-C. Wang, C.H. Li, S.W. Liu, Synergetic molecular oxygen activation and catalytic oxidation of formaldehyde over defective MIL-88B(Fe) nanorods at room temperature, *Environ. Sci. Technol.* 55 (2021) 8341–8350, <https://doi.org/10.1021/acs.est.1c01277>.
- [45] J.W. Ye, B.C. Zhu, B. Cheng, C.J. Jiang, S. Wageh, A.A. Al-Ghamdi, J.G. Yu, Synergy between platinum and gold nanoparticles in oxygen activation for enhanced room-temperature formaldehyde oxidation, *Adv. Funct. Mater.* 32 (2021), 2110423, <https://doi.org/10.1002/adfm.202110423>.
- [46] M. He, Y.Q. Cao, J. Ji, K. Li, H.B. Huang, Superior catalytic performance of Pd-loaded oxygen-vacancy-rich TiO₂ for formaldehyde oxidation at room temperature, *J. Catal.* 396 (2021) 122–135, <https://doi.org/10.1016/j.jcat.2021.01.035>.
- [47] Z.X. Yan, Z.H. Xu, J.G. Yu, M. Jaroniec, Enhanced formaldehyde oxidation on CeO₂/AlOOH-supported Pt catalyst at room temperature, *Appl. Catal. B* 199 (2016) 458–465, <https://doi.org/10.1016/j.apcatb.2016.06.052>.
- [48] X.Q. Yang, X.L. Yu, M.Y. Lin, M.F. Ge, Y. Zhao, F.Y. Wang, Interface effect of mixed phase Pt/ZrO₂ catalysts for HCHO oxidation at ambient temperature, *J. Mater. Chem. A* 5 (2017) 13799–13806, <https://doi.org/10.1039/c7ta03888g>.
- [49] Y. Wang, J. Ye, C. Jiang, Y. Le, B. Cheng, J. Yu, Hierarchical NiMn₂O₄/rGO composite nanosheets decorated with Pt for low-temperature formaldehyde oxidation, *Environ. Sci. Nano* 7 (2020) 198–209, <https://doi.org/10.1039/c9en00652d>.
- [50] D. Chen, Z.P. Qu, Y.H. Sun, K. Gao, Y. Wang, Identification of reaction intermediates and mechanism responsible for highly active HCHO oxidation on Ag/MCM-41 catalysts, *Appl. Catal. B* 142 (2013) 838–848, <https://doi.org/10.1016/j.apcatb.2013.06.025>.
- [51] Y.J. Liang, X. Wu, X.Y. Liu, C.H. Li, S.W. Liu, Recovering solar fuels from photocatalytic CO₂ reduction over W⁶⁺-incorporated crystalline g-C₃N₄ nanorods by synergetic modulation of active centers, *Appl. Catal. B* 304 (2022), 120978, <https://doi.org/10.1016/j.apcatb.2021.120978>.
- [52] C. Zhang, F. Liu, Y. Zhai, H. Ariga, N. Yi, Y. Liu, K. Asakura, M. Flytzani-Stephanopoulos, H. He, Alkali-metal-promoted Pt/TiO₂ opens a more efficient pathway to formaldehyde oxidation at ambient temperatures, *Angew. Chem. Int. Ed.* 51 (2012) 9628–9632, <https://doi.org/10.1002/anie.201202034>.
- [53] D. Yang, S.O. Odoh, T.C. Wang, O.K. Farha, J.T. Hupp, C.J. Cramer, L. Gagliardi, B. C. Gates, Metal-organic framework nodes as nearly ideal supports for molecular catalysts: NU-1000- and UiO-66-supported iridium complexes, *J. Am. Chem. Soc.* 137 (2015) 7391–7396, <https://doi.org/10.1021/jacs.5b02956>.